This article was downloaded by:
On: *14 January 2011*
Access details: *Access Details: Free Access*
Publisher *Taylor & Francis*
Informa Ltd Registered in England and Wales Registered Number: 1072954 Registered office: Mortimer House, 37-41 Mortimer Street, London W1T 3JH, UK

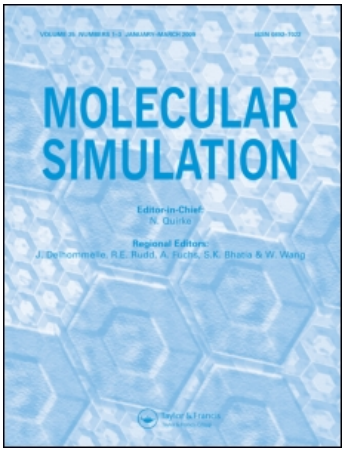

Molecular Simulation
Publication details, including instructions for authors and subscription information:
http://www.informaworld.com/smpp/title~content=t713644482

Application of molecular dynamics DL_POLY codes to interfaces of inorganic materials

P. Martin[a]; D. Spagnoli[a]; A. Marmier[a]; S. C. Parker[a]; D. C. Sayle[b]; G. Watson[c]
[a] Department of Chemistry, University of Bath, Bath, UK [b] Defence Academy of the United Kingdom, Cranfield University Shrivenham, Swindon, UK [c] School of Chemistry, Trinity College, University of Dublin, Dublin, Ireland

To cite this Article Martin, P. , Spagnoli, D. , Marmier, A. , Parker, S. C. , Sayle, D. C. and Watson, G.(2006) 'Application of molecular dynamics DL_POLY codes to interfaces of inorganic materials', Molecular Simulation, 32: 12, 1079 — 1093
To link to this Article: DOI: 10.1080/08927020601013817
URL: http://dx.doi.org/10.1080/08927020601013817

PLEASE SCROLL DOWN FOR ARTICLE

Full terms and conditions of use: http://www.informaworld.com/terms-and-conditions-of-access.pdf

This article may be used for research, teaching and private study purposes. Any substantial or systematic reproduction, re-distribution, re-selling, loan or sub-licensing, systematic supply or distribution in any form to anyone is expressly forbidden.

The publisher does not give any warranty express or implied or make any representation that the contents will be complete or accurate or up to date. The accuracy of any instructions, formulae and drug doses should be independently verified with primary sources. The publisher shall not be liable for any loss, actions, claims, proceedings, demand or costs or damages whatsoever or howsoever caused arising directly or indirectly in connection with or arising out of the use of this material.

Molecular Simulation, Vol. 32, Nos. 12–13, 15 October–15 November 2006, 1079–1093

Taylor & Francis
Taylor & Francis Group

Application of molecular dynamics DL_POLY codes to interfaces of inorganic materials

P. MARTIN†*, D. SPAGNOLI†, A. MARMIER†, S. C. PARKER†§, D. C. SAYLE‡‖ and G. WATSON¶#

†Department of Chemistry, University of Bath, Claverton Down, Bath BA2 7AY, UK
‡Defence Academy of the United Kingdom, Cranfield University Shrivenham, Swindon SN6 8LA, UK
¶School of Chemistry, Trinity College, University of Dublin, Dublin Dublin 2, Ireland

(Received August 2006; in final form September 2006)

Three recent applications of the DL_POLY molecular dynamics code are described, which demonstrate the flexibility and viability of the code for extending our understanding of the structure, stability and reactivity of ceramics and minerals at the atomic level. The first is an investigation into differences in oxygen atom mobility in bulk and at the most stable {111} surface of ceria. The results show enhanced surface transport but that it is via subsurface oxygen. Secondly, we investigate how polychloro-dibenzo-pdioxins (PCDDs) molecules might adsorb on clay surfaces. The resulting adsorption energies show a clear relationship with chlorine content of the molecule. Finally, we apply DL_POLY to comparing the aggregation of magnesium oxide and calcium carbonate nanoparticles. We find that very small calcium carbonate nanoparticles are amorphous and their aggregation shows no preferred orientation in contrast to magnesium oxide, which remain highly crystalline and combine in a highly structural specific way.

Keywords: Molecular dynamics; DL_POLY; PCDDs; Inorganic materials; Oxygen migration; Adsorption; Aggregation

Downloaded At: 17:58 14 January 2011

1. Introduction

The aim of this paper is to describe our current work using DL_POLY to model the structures and energetics of inorganic solids, with particular emphasis on surfaces and nanostructures. We illustrate the scope of DL_POLY to modelling surfaces and interfaces by considering three recent examples. The first example describes our application of DL_POLY to explore the stability and transport of surface defects, oxygen vacancies on the most stable surface of ceria. Understanding the factors controlling the formation of surface defects is of importance for understanding surface properties. As it is the surface defect that is often the site of chemical activity. Surface defects can also include adsorbed molecules and in our second example we are following the DFT work by the Cambridge group [1] by applying DL_POLY to help our understanding of adsorption processes. Nanoparticles are of great scientific interest as they are effectively a bridge between bulk materials and atomic or molecular structures. The interesting and sometimes unexpected properties of nanoparticles are partly due to their large number of surface sites aspects. The percentage of atoms at the surface of a material becomes significant as the size of that material approaches the nanoscale. Thus in our final example we describe recent work on studying the structure and aggregation of nanoparticles of two minerals.

2. Molecular dynamics at the stable low index {111} surface of ceria

Materials based on ceria (CeO_2) are used in the production and purification of hydrogen, the purification of exhaust gases in three-way automotive catalytic converters, and other catalytic applications [2–5]. These applications make use of the unusual properties of ceria, namely, the ability to shift between its two oxidation states, Ce(III) and Ce(IV), and the high mobility of bulk oxygen species—properties that allow ceria to behave as an oxygen buffer. It is important

*Corresponding author. Email: chppm@bath.ac.uk
§Tel.: +44-1225-386505. Fax: +44-1225-386231. Email: s.c.parker@bath.ac.uk
‖Tel.: +44-1793-785264. Fax: +44-1793-785772. Email: d.c.sayle@cranfield.ac.uk
#Tel.: +353-1-608-1357. Fax: +353-1-671-2826. Email: watsong@tcd.ie

Molecular Simulation
ISSN 0892-7022 print/ISSN 1029-0435 online © 2006 Taylor & Francis
http://www.tandf.co.uk/journals
DOI: 10.1080/08927020601013817

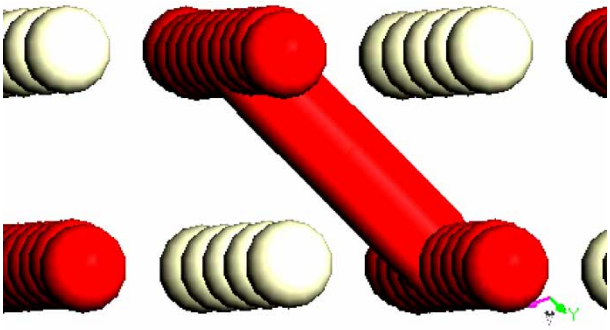

Figure 1. Oxygen atom migrating in the middle of {111} surface slab.

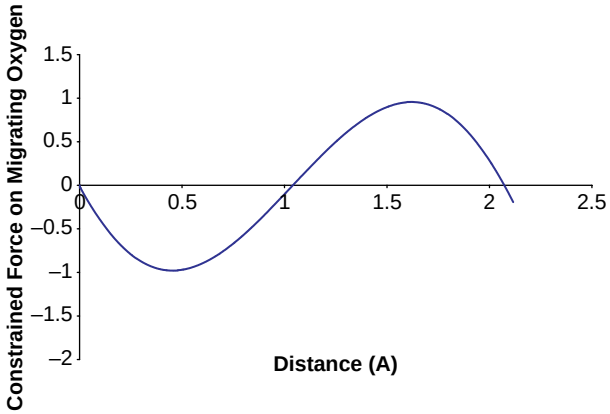

Figure 3. Plot showing constrained force experienced by the migrating atom over distance travelled in bulk ceria.

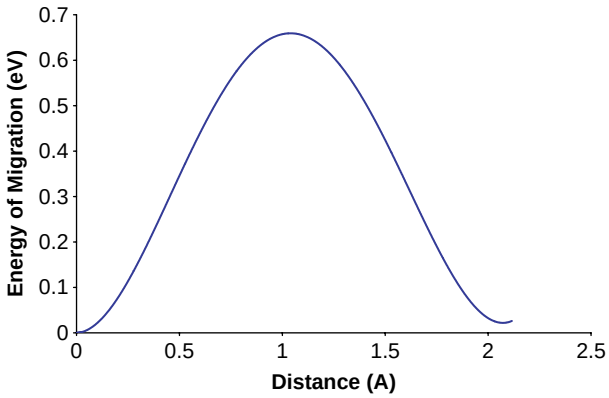

Figure 2. Energy profile of bulk oxygen migration.

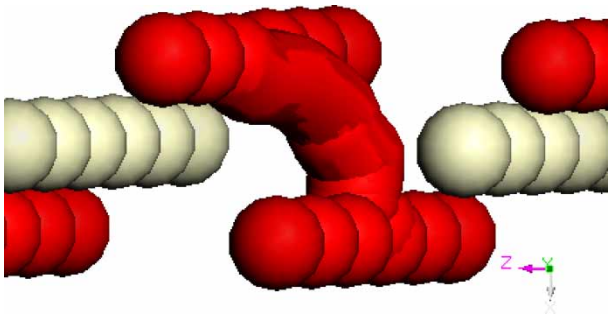

Figure 4. Oxygen atom migrating in the {111} surface.

therefore that we understand more fully how oxygen atoms move in the ceria surface. In this study, we focused on studying transport at or near the {111} surface of ceria, chosen because it is the most stable surface [8] and hence most prevalent.

The minimum energy techniques applied to dislocation, interface and surface energies code (METADISE) [6] was used to construct the surface slabs for DL_POLY.

A slab of the {111} surface was constructed to a thickness of 20.6 Å, which is sufficiently thick to allow realistic simulation of bulk ceria at the centre of the slab. The slab contains 996 atoms. 332 Ce, 664 O. We chose to use 3D periodicity for computational ease and hence introduced a 50 Å vacuum gap. The Coulombic sums were calculated using Ewald summation precision of 10^{-5}, which provides a straightforward way of specifying the number of reciprocal lattice vectors and indicates the precision to which the reciprocal component of the Ewald sum is converged.

The potential model used in this work was derived by Balducci *et al.* [7] and is a modification of a potential derived by Sayle [8]. We included the shell model of Dick and Overhauser [9] to simulate ionic polarizability of the oxygen ions. In this model, the oxygen ion is represented as a core plus a shell coupled by a harmonic spring. The total charge is separated between the shell and the core. In the molecular dynamics (MD) simulations the shells were given a mass of 0.5 au.

In order to investigate oxygen atom mobility at the stable {111} ceria surface a potential of mean force (PMF) method modification to DL_POLY [10] has been used to simulate the pathway and variation in free energy of a single oxygen atom migrating in bulk ceria and also at the surface.

The constrained atom is moved towards a vacancy at a constant velocity. The velocity chosen was 100 m/s, which is fast enough to obtain good statistics in sufficient CPU time but slow enough to allow the neighbouring ions to relax while the atom is migrating. Slower velocities did not make a significant difference to the energy profile.

$$\Delta A(z) = A(z) - A(z_0) = \int_{z_0}^{z} f_z \, \mathrm{d}z \tag{1}$$

f_z : average force in direction of vacancy.

The constrained atom is given a target vector, which is the co-ordinates of the lattice vacancy position. However, the constrained atom is free to move perpendicular to the target vector. The average force of the constrained atom along the target vector is recorded at the end of each time-step. Integration of the force with respect to distance yields the free energy, shown in equation (1), $\Delta A(z)$ is the free energy change of migration, $A(z)$ is the free energy at position z and $A(z_0)$ is the free energy at the initial position.

Downloaded At: 17:58 14 January 2011

Thus the free energy of atom migration can be calculated at various temperatures. Additionally, DL_Poly can be run just above zero Kelvin to enable the identification of the pathway and energy change neglecting temperature. This allows for simple (or an initial) analysis of the migration process, without involving complications of nearby atoms excessively hindering the constrained atom during its trajectory. In doing this, entropy effects are ignored, and therefore the energy of migration rather than the free energy of migration, is in fact calculated.

Migration of a single oxygen atom was investigated at the centre of the slab, which represents bulk ceria; just beneath the surface, with an oxygen migrating between bulk and a vacancy position just under the surface; and at the surface, where oxygen migration is simulated between the layer of oxygen atoms just beneath the surface and the surface layer, and also the migration from a surface position to a near surface vacancy.

3. Oxygen migration

The first PMF simulations were carried out on the diffusion of oxygen in the bulk of the slab. We initially assumed that a vacancy was formed without a localised charge compensation, which we envisage as modelling the transport of the unbound oxygen vacancy. The slab was initially run at 300 K using the NVT ensemble, and the migration path plotted. The results show that the pathway between oxygen sites is linear (figure 1) and that the energy of migration is 0.66 eV with the transition state half way between the oxygen sites, see figure 2. The activation energy agrees very well with the work of Balducci *et al.* [11] who calculated 0.65 eV using a series of static energy calculations.

We can check that the location of the transition state is exactly halfway between the sites by plotting the average force of the constrained atom in the direction of travel in figure 3. The force passes through zero at 1.05 Å along a total distance of 2.07 Å.

We next modelled the trajectory for an oxygen atom migrating from the oxygen layer just below the surface to a vacant site on the surface.

Figure 4 shows the pathway. The first point to notice is the trajectory is now curved.

The energy plot in figure 5 shows also a marked asymmetry. The transition state in this case is very close to the surface ∼0.5 Å. Furthermore, figure 5 shows that the activation energy for the oxygen migration from the surface to the level just beneath is considerably smaller, i.e. 0.06 eV. Interestingly, a greater activation energy, 0.3 eV, is required to activate the return of a subsurface oxygen directly to the {111} surface from this layer beneath, which is still less than 0.66 eV, the bulk value. It also clearly demonstrates that the vacancy is more stable just below the surface.

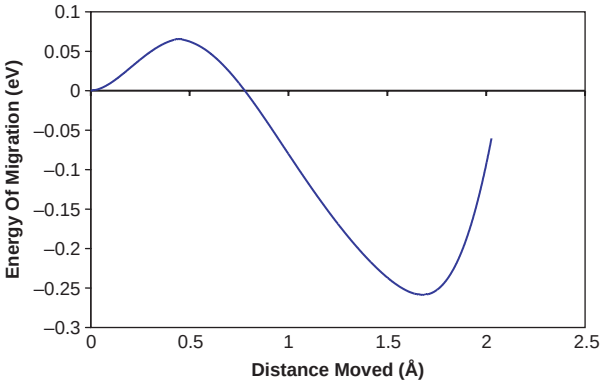

Figure 5. Energy profile of oxygen migration in the {111} surface.

The next stage was to examine the transport from the surface layers to the bulk. Figure 6 suggests the barrier is 0.67 eV, with the sub-surface site 0.2 eV less stable.

Analysis of the trajectory shows that the migration path is not linear as in the bulk simulation, and that the position of the transition state is predicted to be slightly closer to the bulk layer than the sub-surface layer.

We also considered the migration of an oxygen atom across the top of the surface and surprisingly found that the activation energy was 2.5 eV. Thus figure 7(a),(b) illustrates how a migrating oxygen atom would move down a layer just under the surface, and then would return to the surface layer leaving a vacancy in the sub-surface layer. This is the most stable site for an isolated vacancy, rather than transport across the surface, which is not unlike the recently proposed mechanism for surface transport by Allan and Harding [12].

We have seen more complex behaviour in some of the simulations, but still involving oxygen movement between the top two layers. Figure 8 shows the initial configuration of a concerted mechanism involving an oxygen atom in the surface layer constrained to move down into a vacancy position just under the surface. The initial constraint is shown by the largest green arrow in order. The constrained migration results in the formation of a vacancy in a less stable position on the surface because vacancies are more stable at a position just under the surface. The result is that, as the constrained oxygen leaves its lattice site to

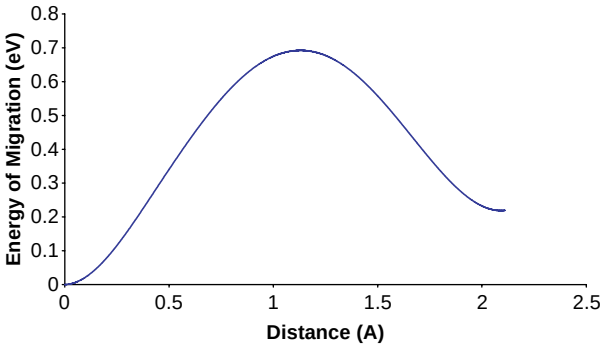

Figure 6. Energy profile of oxygen migration from bulk to just under the {111} surface.

Downloaded At: 17:58 14 January 2011

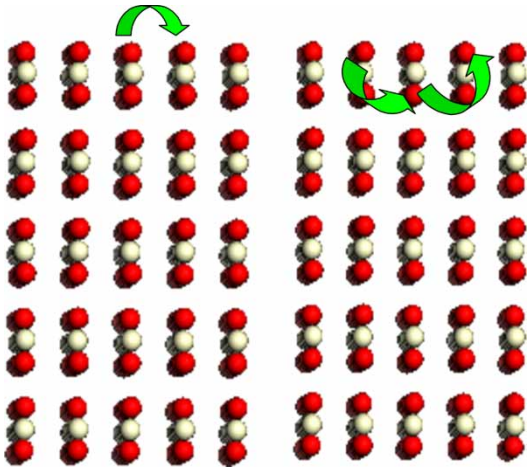

Figure 7. (a) Schematic of oxygen hopping across the surface; (b) schematic of oxygen moving through the surface.

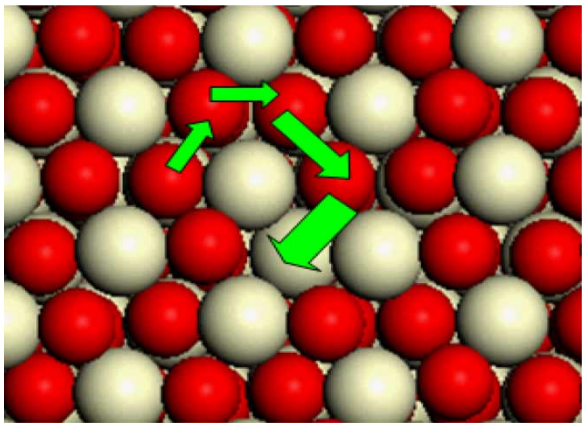

Figure 8. Pathway of concerted mechanism.

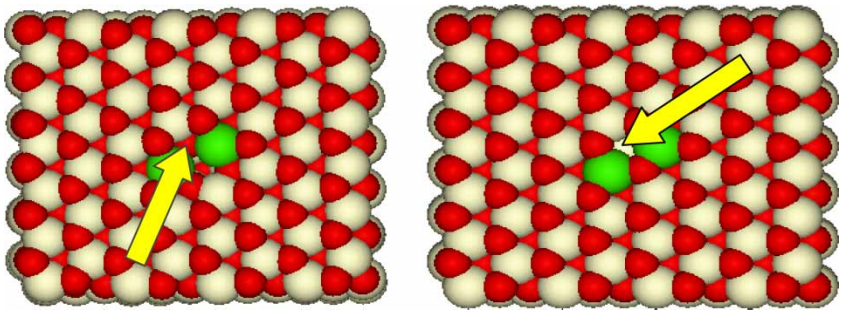

Figure 9. (a) Before migration and with surface vacancy in place; (b) after migr oxygen atom, originally under the surface between Ce^{3+} ions, has migrated to the surface leaving vacancy just under the surface and between Ce^{3+} ions.

Downloaded At: 17:58 14 January 2011

form a vacancy we find that the next oxygen atom fills the empty site and because the energy barriers are so low the next few oxygen atoms move in unison. The net result is that a sub-surface vacancy is formed but can be potentially some distance from the original vacancy.

The concerted motion does however highlight one problem, namely that the movement of the ions in the concerted mechanism causes a resistance to the movement of the constrained atom, thus the resulting free-energy change is the sum of the activation free energies of migration and the free energy for overcoming the drag-force. Thus care must be taken in interpreting the activation free energy.

Another important issue is the effect of charge compensation particularly when the charge compensating defects are bound to the oxygen vacancies. We consider them in the following section.

We treated the charge compensating defects as localised electrons on neighbouring cerium ions. Thus we first considered (figure 9(a)) the oxygen atom migrating directly into a vacant site, which is adjacent to two Ce^{3+} ions. The trajectory of migration takes the oxygen between the two adjacent Ce^{3+} ions. The effect of the charge compensating Ce^{3+} ions on the migration is significant. The new activation energy is 1.35 eV (figure 10), compared to 0.06 eV for similar migration without the involvement of compensating ions.

Another interesting result of this calculation is that the final configuration, with the vacancy just below the surface is calculated to be 0.4 eV less stable. But note that the final oxygen vacancy position is not in the highly bound state (i.e.) just under the surface and adjacent to the charge compensating Ce^{3+} ions.

The second example (figure 11(a)) considered is where an oxygen atom just beneath the surface is forced to migrate to a surface site that is adjacent to both, the vacancy and a compensating Ce^{3+} ion, i.e. the oxygen vacancy moves from the top layer to the layer underneath. In this case, the activation energy of migration (figure 12) is similar to that for the un-charged compensated migration, i.e. 0.10 eV cf. 0.06 eV.

The activation energy for the reverse process is approximately 1.0 eV, thus in common with the un-charged compensated migration, the vacancy is more stable below the surface but is very much more stabilised, i.e. by about 0.9 eV.

Hence, the energetics for the migration of an oxygen atom into a bound charge compensated vacancy cluster, when that oxygen atom approaches the vacancy from the

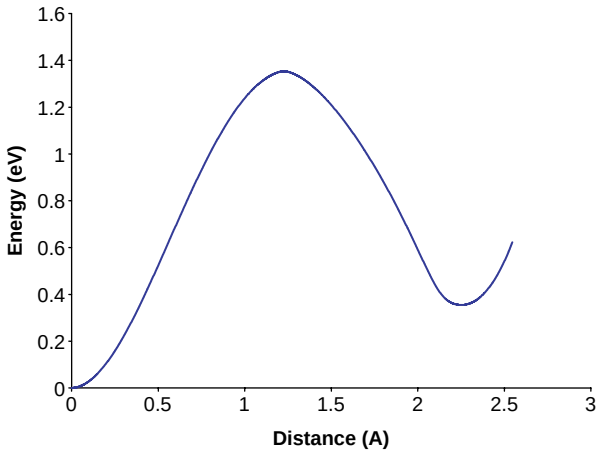

Figure 10. Energy profile of oxygen atom migration between Ce^{3+} ions onto the surface.

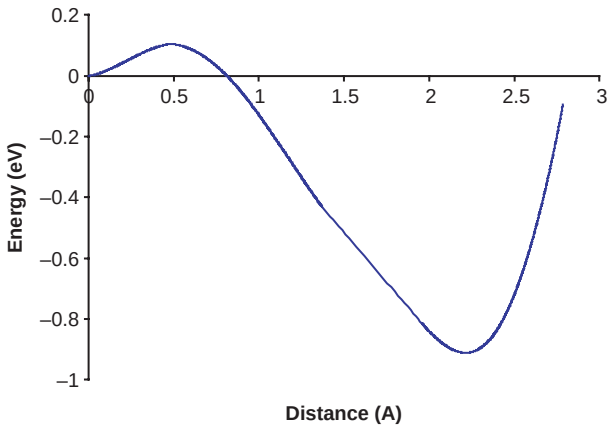

Figure 12. Energy profile of oxygen atom migration from under the left hand Ce^{3+} ion into the surface vacancy between compensating Ce^{3+} ions.

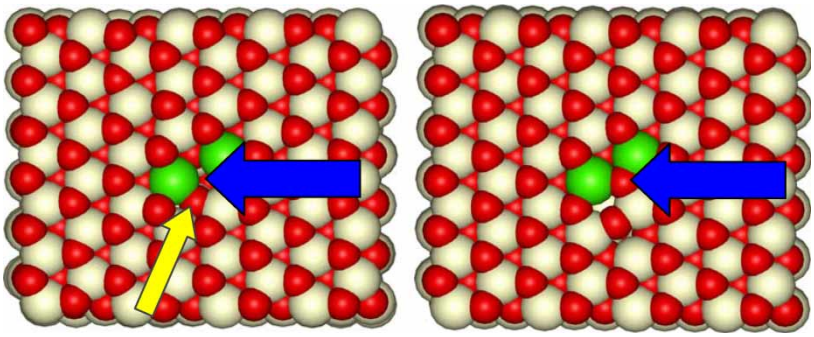

Figure 11. (a) Before migration and with surface vacancy in place; (b) after migration, oxygen atom, originally under the surface and below the vacancy, has migrated to the surface leaving vacancy just under the surface and below the left Ce^{3+} ion.

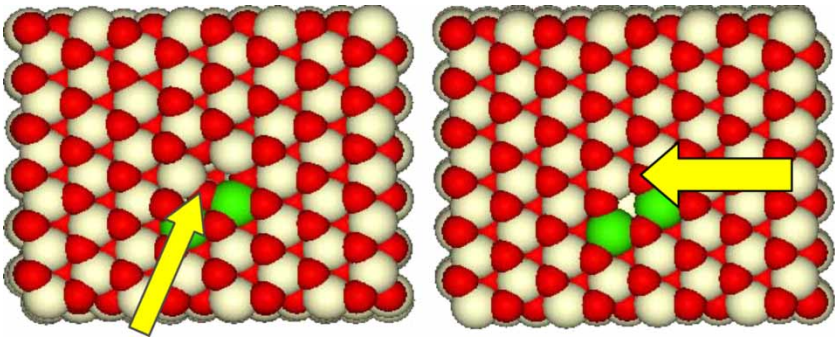

Figure 13. (a) Before migration and with surface vacancy in place; (b) after migration, oxygen atom, originally under the surface between Ce^{3+} ions, has migrated to the surface leaving vacancy just under the surface and between Ce^{3+} ions.

side of the compensation, differ significantly from the case of migration between the compensating ions.

The final example considered (figure 13(a)) involves the migration of an oxygen atom, which is originally under the surface between two adjacent Ce^{3+} ions, to a vacancy position set just to the side of this charge compensating pair of ions. The direction of migration is away from the charge compensation up into the vacancy which is considered here only to be partially bound because the vacancy is not symmetrically configured. Thus the final configuration leaves the vacancy in the highly bound state.

The plot in figure 14 shows that the activation energies are still small, at 0.25 eV for the forward and 0.4 eV for the reverse.

However, activation migration energy is four times greater than the energy for the uncharged compensated case. It is 2.5 times greater than the migration into a bound charge compensated vacancy with a trajectory from the side, but is much smaller than the 1.35 eV required for

Downloaded At: 17:58 14 January 2011

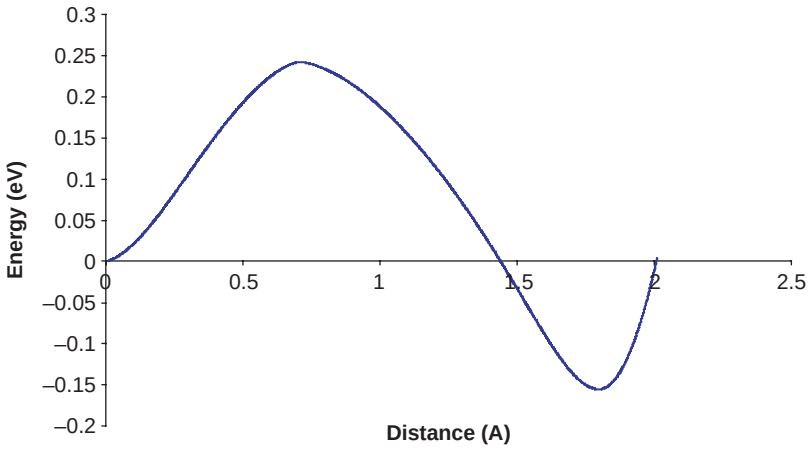

Figure 14. Energy profile of oxygen atom migration from under the left hand Ce^{3+} ion into the surface vacancy between compensating Ce^{3+} ions.

activation of migration up and between charge compensating ions into the fully bound vacancy.

The results show that energetically the vacancy prefers to be bound to the charge compensating defects in the subsurface oxygen site. Furthermore, the location of these charge compensating defects modify the activation energies and hence the mobility of oxygen near the surface. In the case of the movement along the site of the Ce^{3+} ions, the effect is significant and will have a large anisotropic effect on the atom transport.

The results therefore suggest that the migration of a defect cluster differs from isolated defects. Therefore, it is important to investigate the stability of different clusters.

These simulation results suggest an important significance in the direction of migration around or between partially or fully bound charge compensated defects, in that it appears that oxygen atoms prefer to migrate up from the side of a bound compensated surface vacancy.

Lastly, it is important to note that a number of *ab initio* studies, for example Watson *et al.* [13–16], have been performed on ceria. Comparison between the *ab initio* and potential based approaches used here, see for example [17], have shown that the potentials are reliable.

4. Organic molecules adsorbed on clay surface: DL_POLY as a high-throughput engine

Organic pollutants and related molecules can pose a serious environmental threat to the global ecosystem. Amongst the most notorious are halogenated compounds substances used as pesticides or as by-products from other human activities. There are concerns because of their general toxicity and the fact they can enter the food chain, as well as affecting the quality of water, soil and atmosphere. In the absence of well thought remediation plans, risk management strategies can give information needed to allow stakeholders to decide options concerning disposal of these potentially harmful chemicals.

There have been numerous investigations involving the modelling of clay surfaces and adsorption of organic species [18–21]. However, our interest lies in the understanding of how these molecules might bind to mineral surfaces and in establishing a high-throughput methodology that can efficiently investigate the many possible combinations of molecules with substrates.

As a starting point, we choose the polychloro-dibenzo-pdioxins (PCDDs) family. The 76 members of this family (namely, congeners) have a different number of chlorine atoms replacing hydrogen atoms at different positions.

We then choose a clay substrate, of relevence to soils. The di-octahedral 2:1 sheet silicate pyrophillite, $Al_4Si_8O_{20}(OH)_4$ is a simple example of the family of clay minerals that form a significant fraction of many soil and rock types. Its [001] face was first considered.

Preliminary DFT calculations showed that the organic molecules do not chemisorb on the pyrophillite surface. Of course, DFT is not adapted to the accurate study of physisorption phenomena due to its poor treatment of dispersion. Therefore our potential based method was deemed ideal for such a study.

We now describe the choices of models, tools and resources, and then follow with a brief discussion of the automatisation procedures and comments on the scientific results.

5. Model

A classical model requires an electrostatic description of atoms as well as a parameterisation of the intra-molecular and the inter-molecular interactions.

Well established models for Zeolite and clay minerals make modeling the substrate a comparatively straightforward task. We chose the parameterisation of Lewis and Catlow [22] in which the electrostatics is described by the shell model of Dick and Overhauser [9]. The total charge is separated between the shell and the core. In the MD simulations the shells were given a mass of 0.5 au.

Downloaded At: 17:58 14 January 2011

For the molecules, we chose the CVFF model [23] for the bonding interactions. The attribution of the electrostatic components was more complex. We used *ab initio* calculations (Gaussian code [24]) with the Dunning/Huzinaga valence double-zeta basis set on selected PCDDs'. From these we extracted the charge distribution to extrapolate point charges for all the PCDD. This simplified charge model is described in table 1.

We generated the interaction parameters between the substrate and the adsorbed molecules by using the standard combination rules, which is a valid approach to obtain dispersion-repulsion interaction coefficients in the absence of strong bonding.

Our confidence in this model is confirmed by the excellent agreement of test calculations on the adsorption of simpler molecules (linear and cyclic aliphatic hydrocarbons) with experimental measurements [18,25]: in the case of cyclohexane, $-57\,\mathrm{kJ\,mol^{-1}}$ compared to $-54\,\mathrm{kJ\,mol^{-1}}$ at 423 K.

6. DL_POLY as an optimiser

DL_POLY is the UK's national flagship package for MD simulations [26]. While it is especially good for simulating very large systems, its modular structure makes it very adaptable. It supports some form of energy optimisation (albeit not as efficiently as specialist codes such as GULP [27] or METADISE [6]). It is also cml enabled which allows for certain direct inter-operability with some DFT codes.

The choice of a MD code for a problem essentially based on optimisation might appear to be odd at first. However, our main objective is to tackle adsorption in realistic conditions, i.e. at various temperatures and with the involvement of water. MD is the tool of choice for these more advanced problems. So, to maintain upward compatibility, we decided to use the same code for the current study as we would for the more advanced one, even though there is added complexity using a MD code to perform optimisation.

Additionally, the choice was justified because the force field involved was designed with the aspects of the larger study in mind and is therefore relatively complex and not adaptable to GULP or METADISE codes without heavy recoding.

7. UCL condor pool

This project is combinatorial in nature. That is, not only are there 76 non equivalent PCDD molecules, but the determination of reliable adsorption sites requires multiple starting configurations. Furthermore, the search space is large and the potential energy surface can be complex and thus contains many local minima. However, the systems are not overly large and each energy calculation is not too computationally demanding. A brute force approach to optimisation is therefore deemed appropriate and indeed, affordable.

Instead of using a supercomputer, we took advantage of the UCL Condor pool. This type of resource is ideal for this study, as it contains a very large amount of processors (at the time of writing 960 CPUs, operating under Windows OS).

Another feature of the Condor setup is the DAGMAN workflow manager which allows complex workflows. In our case, it essentially made the analysis task automatic.

8. Methodology

First of all, three sets of independent calculations are required: molecule only (M), substrate only (S), molecule adsorbed on substrate (M + S). The adsorption energy is defined as a difference between the energy of these systems ($E_{MS-EM-E_S}$).

The two custom files node_list and atom_list are at the centre of the data structure and operate on the two modified DL_POLY input files FIELD and CONFIG. node_list contains 76 lines, one for each PCCD, starting with a user provided molecule code, and then twenty two intermediate atom codes, in the order in which the atoms appear in the CONFIG file (these codes can be H, Cl, O, C, CH, CCl or CO). atom_list creates a link between these intermediary codes and the names used in the CONFIG (H, Cl, O, C), as well as with the charges appearing in the FIELD file (as the carbon atoms can be allocated different charges). It also contains information concerning the bonding parameters, which need to be allocated in the FIELD file.

A list of dedicated scripts reads the node_list and operates on the 76 corresponding directories.

The simpler scripts are just expansions of unix commands (list_cp, list_mv, list_grep). list_setdir generates the data structure (directories NODE_n-molecule-code, where n is an arbitrary molecule index, corresponding to the order in node_list). list_config replaces $<$ list $>$ flags in a modified CONFIG by the correct atom name and put the correct CONFIG in its directory. list_field replaces $<$ list $>$ and $<$ harm $>$ flags in the field by their value from the atom_list (atom name and charge, two specie bonds parameters). list_fire submit the jobs to the condor scheduler (via run.dlp files). list_rota, is an expanded version of list_config which additionally applies a rotation and/or translation to the flagged atoms of CONFIG (in our case of course those of the PCDD molecule).

Table 1. Charge model (in e).

Specie	Charge (e)
H	0.20
Cl	−0.03
O	−0.50
C (H bonded)	−0.20
C (Cl bonded)	0.03
C (O bonded)	0.25

Downloaded At: 17:58 14 January 2011

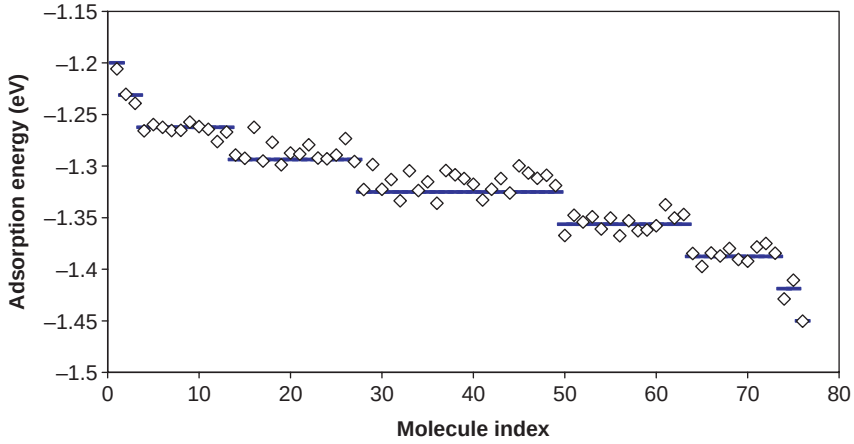

Figure 15. Adsorption energy of the 76 PCDD.

These scripts are sufficient to optimise the structures of the isolated molecules.

As already mentioned, the case of the adsorbed molecules is slightly more complex as several starting configuration are needed. Each of these is carried sequentially, for each molecule. The script config_rota, a same directory, command line version of list_rota is used in conjunction with DAGMAN. list_fire is also updated to list_fire_dag. Practically, three sites of high symmetry were explored (above Si, above O, above "hexagon" centre, see figure 16) with eight rotational configuration (by increment of pi/2), with 24 calculations per molecule.

9. Results and discussion

In figure 15 we plot the adsorption energy of the 76 PCDDs. The molecule index is only meaningful in so far as it increases with the number of chlorine atoms. The horizontal lines are a guide for the eye and correspond to molecules with the same number of chlorine. It can be seen that the adsorption energy is strongly correlated to the number of chlorine. Each additional chlorine attached to the carbon rings leads on average to an adsorption energy increase of 0.03 eV.

Furthermore, and as might have been expected, all of the molecules lie flat on the surface, see figure 16.

We also observe that corrugation energy increases with the number of chlorine. The potential energy surface is very flat for the PCDD with a low Cl count (indeed the translational corrugation energy is 0 ± 0.01 eV for $C_{12}O_2H_8$). At higher Cl count, the corrugation increases, up to 0.07 eV for $C_{12}O_2Cl_8$. Therefore, the concept of the adsorption site is rather meaningless for molecules with numbers of Cl lower than 4. For molecules with greater than 3 Cl atoms, the PCDD almost systematically favours a position such as illustrated in figure 16, with the centre of mass of the molecule situated above a surface oxygen, and where the benzene rings sit inside the quasi-hexagon of the surface top layer.

As well as the modelling of molecules that are in contact with surfaces, we are also concerned with the interaction of nanoparticles.

10. Molecular dynamics simulations of the structural changes that occur during aggregation of mineral oxide and carbonate nanoparticles

DL_POLY has been used by other groups to study the structure and stability on minerals on the nano-scale. Spano *et al.* found computational evidence of ZnS forming bubble type clusters [28] $(ZnS)_n$ clusters, with n ranging from 10 to 47, were energy minimised using a simulated annealing technique. Spano *et al.* found that spheroidal (bubble) clusters with only three coordinated atoms are more stable than the bulk structure. If the number of ZnS units is increased to 60 then the appearance of onion structures occur [29]. This is a $(ZnS)_{12}$ inside a bubble of

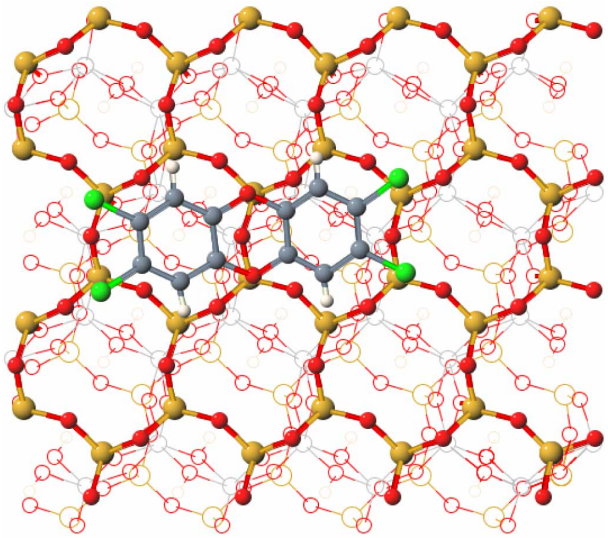

Figure 16. Adsorption position of a PCDD congener. The surface is parallel to the page. The shaded atoms represent the lower layers. Surface: Si large light grey, O small dark grey. Molecule: H white, Cl light grey, C grey, O dark grey.

Downloaded At: 17:58 14 January 2011

Downloaded At: 17:58 14 January 2011

$(ZnS)_{48}$. Banfield and co workers have also considered ZnS nanoparticles, typically $n = 360–400$, making the diameter of the ZnS crystal around 3 nm, which is comparable to experimental synthesised particles [30]. The Banfield group started using MD to study the phase stability of ZnS nanoparticles in vacuum and in the presence of water. They found that the wurtzite (ZnS) nanoparticles smaller than 7 nm are more stable than sphalerite nanoparticles in vacuum at 300 K. However adsorption of water onto the ZnS nanoparticle surface stabilizes the sphalerite structure. Zhang *et al.* [31] predicted anhydrous ZnS nanoparticles to have a highly disordered structure. Again these nanoparticles had a diameter of around 3 nm. The adsorption of water, however, onto the nanoparticle surface results in the formation of a relatively crystalline core. Zhang and Banfield showed that this phase transformation of sphalerite to wurtzite could be caused by nanoparticle aggregation and coarsening [32]. These 3 nm ZnS nanoparticles were randomly orientated with respect to each other and allowed to aggregate to form a larger nanoparticle. Following aggregation the coarsened particle adopts a near-amorphous structure that transforms rapidly to wurtzite. This work by Banfield and co-workers has provided a link between atomistic simulation and the forces that cause their aggregation, i.e. colloidal chemistry. We have used DL_POLY to extend the range of materials to simulate the aggregation process of two different materials, MgO and calcite ($CaCO_3$) nanoparticles. First we will describe the potentials used to describe the interatomic interactions and then describe how we set up our systems for aggregation.

The potential model used for simulating the magnesium-oxygen interaction is that of Lewis and Catlow [33] and has been used before to simulate MgO surfaces [34,35] and MgO nanocrystals [36]. The potential model used for simulating the calcium-carbonate interactions in calcite is that of Pavese *et al.* [37] and has been used in the past to simulate calcite surfaces [38] and also calcite nanoparticles [39]. All simulations in this section employ the shell model of Dick and Overhauser [9]. Where the shells are in the oxygen species only and have a mass of 0.2 au in $CaCO_3$ and 0.5 in MgO, this represents the electronic charge cloud connected by a harmonic spring to a core containing most of the anion's mass.

We have begun studying the structure and aggregation using MD simulations by modelling an eight nanoparticle system. Each of the nanoparticles in the simulation is the same distance apart. The simulation was performed in vacuum with no periodic boundary conditions. The molecular dynamic simulation was performed in a canonical ensemble at 300 K and ambient pressure using a time step of 0.1 fs. Each simulation was run for 1 ns with a 2 ps equilibration period.

11. Aggregation of magnesium oxide nanoparticles

Each MgO nanoparticle had a 0.6 nm in diameter and the simulation started with them being 2.3 nm apart. The

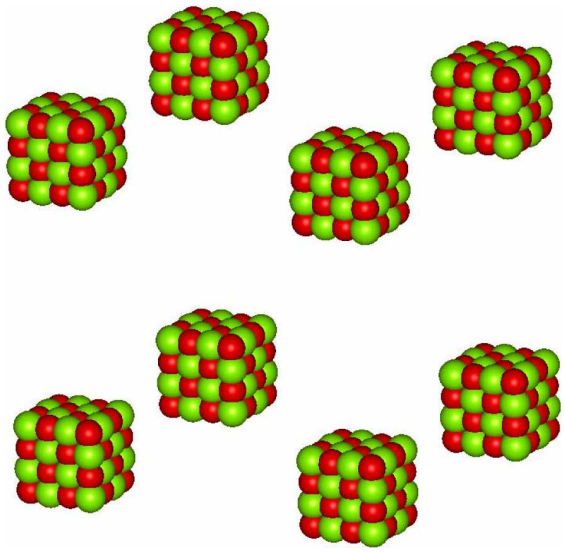

Figure 17. Initial configuration of eight MgO nanoparticles before aggregation.

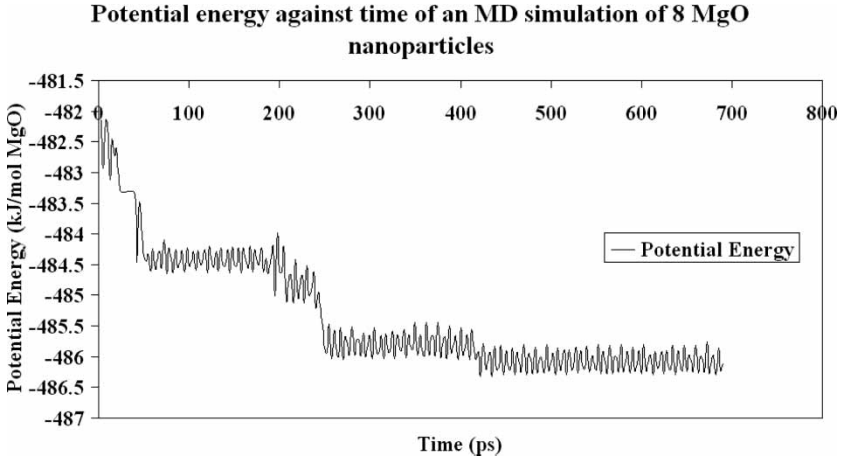

Figure 18. Potential energy per magnesium ion against time of an MD simulation of eight MgO nanoparticles.

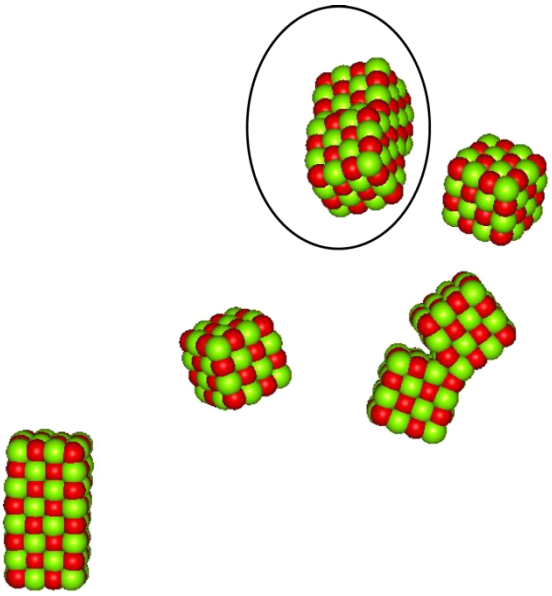

Figure 19. A snapshot of the MD simulation at 30 ps for the MgO system.

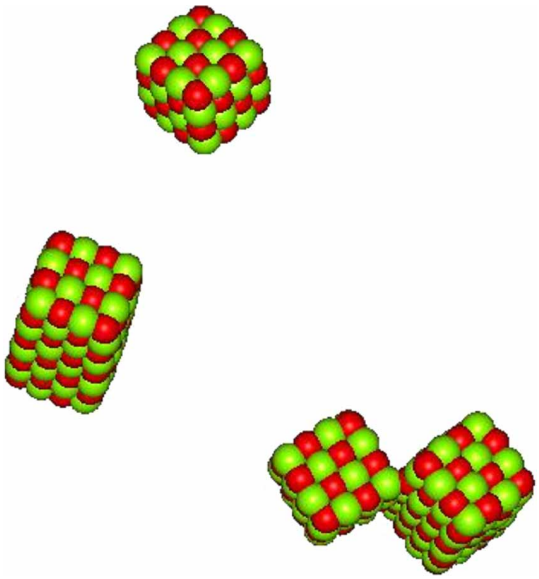

Figure 20. A snapshot of the MD simulation at 60 ps for the MgO system.

starting configuration is shown in figure 17. We have eight cubes of MgO as the most stable surface grows along the {100} plane [6]. We can plot the potential energy of our simulation as it evolves over time (figure 18). The starting configuration has a potential energy of −482.1 kJ/mol of Mg ions and then drops rapidly in-between 30–55 ps and −484.4 kJ/mol. This decrease in potential energy corresponds to the initial aggregation of MgO nanoparticles. Figure 19 shows a snapshot of the MD simulation at 30 ps. The particles retain their bulk-like structure and well ordered surfaces. At 30 ps single MgO nanoparticles are starting to aggregate together in pairs. The aggregation process seems very ordered and is dominated by

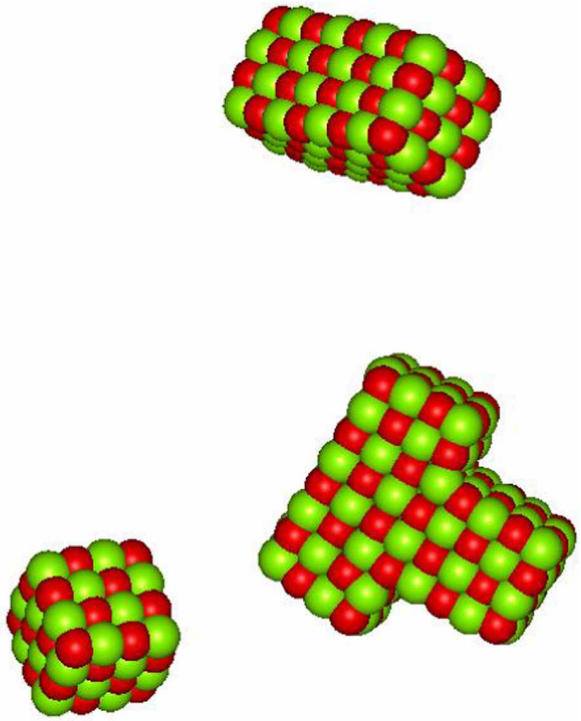

Figure 21. A snapshot of the MD simulation at 220 ps for the MgO system.

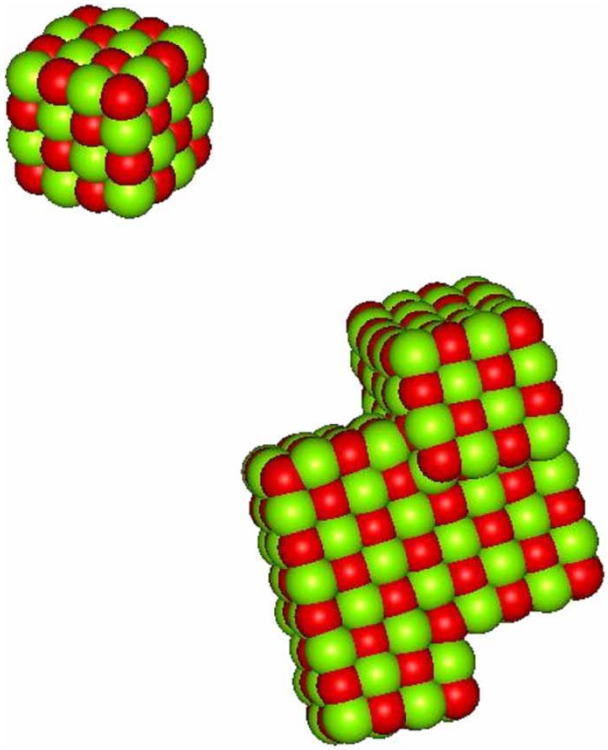

Figure 22. A snapshot of MD simulation at 275 ps for the MgO system.

orientation along the {100} plane. This snapshot is also interesting because it also shows that the merging nanoparticles will join at the corners first. The pair of

Downloaded At: 17:58 14 January 2011

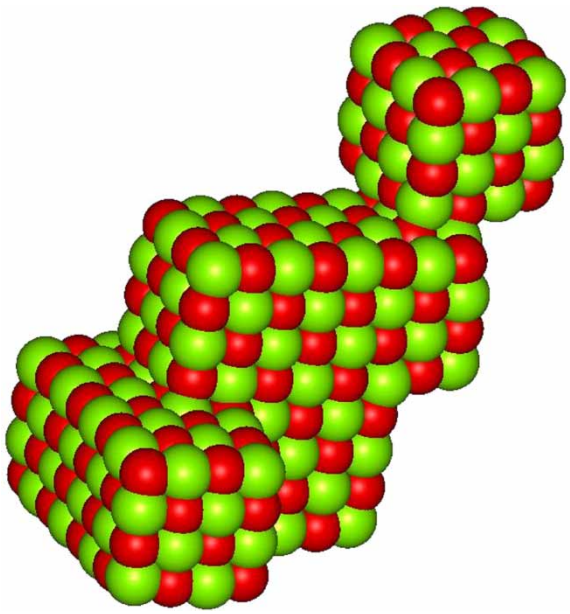

Figure 23. Final configuration of the aggregated MgO nanoparticles.

nanoparticles that are circled in figure 19 are a pair that drifts further and further away from the rest of the nanoparticles and do not aggregate with the other six nanoparticles. Since they are so far away in some of the snapshots it is not practical to show them in some of the pictures. At 60 ps figure 20 shows a stabilisation of potential energy at around −484.4 kJ/mol. Figure 20 shows a snapshot of the MD simulation at 60 ps and shows the aggregation of a single MgO nanoparticle to a pair. The snapshot again illustrates the general result that aggregation has initially occurred along the corners of the nanoparticles. The nanoparticles find their preferred face centre cubic site at 220 ps (figure 21) when the potential decreases to around −484.6 kJ/mol. The increased ordering of aggregation along the {100} plan continues when the potential energy decreases to −485.8 kJ/mol when a pair of nanoparticles aggregate to the triplet at 275 ps (figure 22). The final configuration occurs at 460 ps (figure 23). Here the sixth nanoparticle joins the cluster of five. The two nanoparticles circled in figure 19 were in fact too far away to become attracted to the rest of them.

Downloaded At: 17:58 14 January 2011

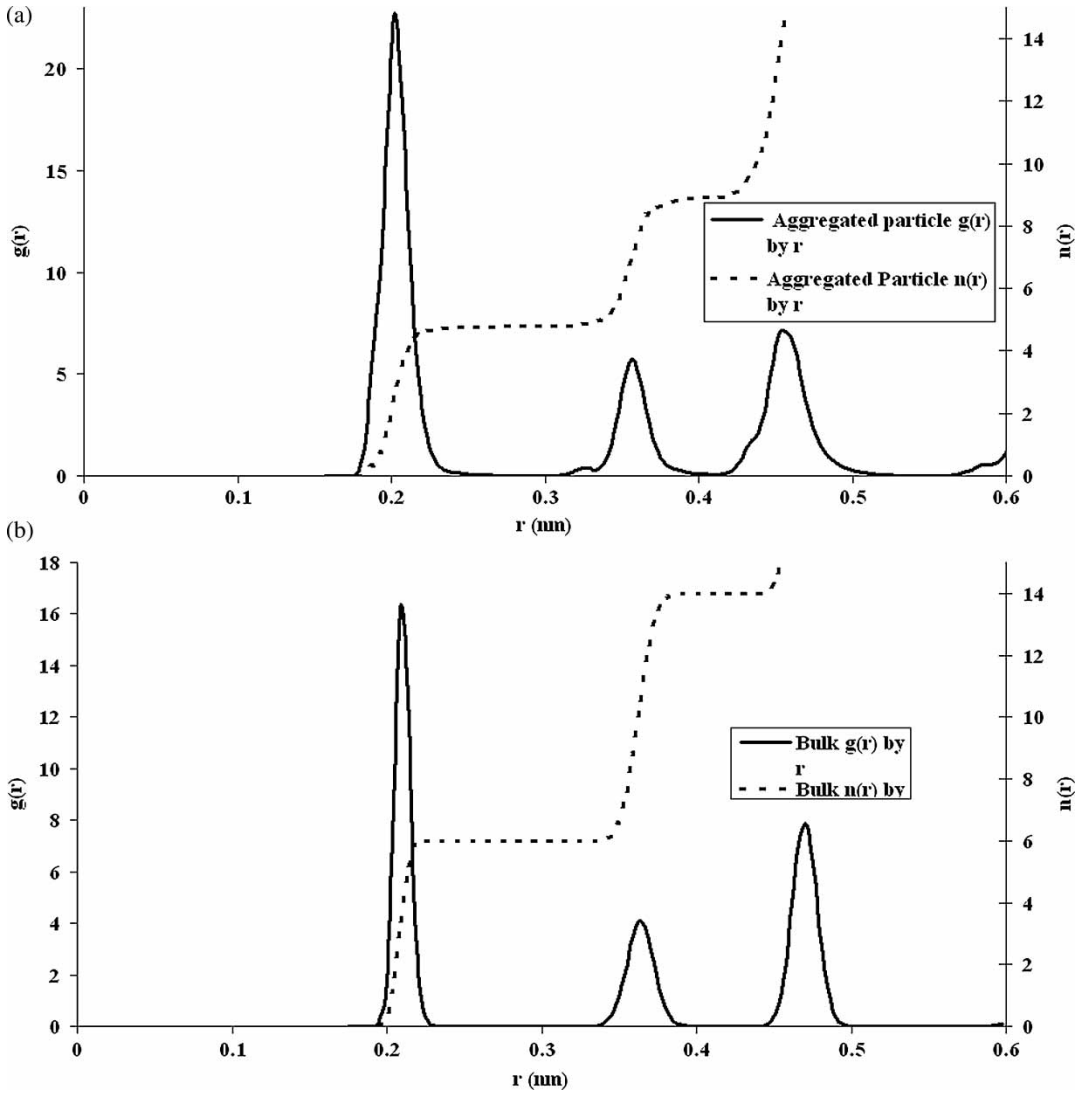

Figure 24. RDF of the (a) aggregated MgO nanoparticles and (b) bulk MgO.

This aggregation process has also shown that when crystal growth occurs in MgO there are the chances of kinks and steps being formed.

We can compare any structural changes that may have occurred during aggregation by comparing the radial distribution functions (RDF) of aggregated nanoparticles with bulk MgO. Figure 24 shows the RDF of the (a) aggregated MgO nanoparticle and (b) bulk MgO. The RDF's of the aggregated MgO nanoparticle and bulk MgO are very similar with the first three peaks showing Mg—O bond distances at 0.21, 0.35 and 0.45 nm in both graphs. These interatomic distances agree with X-ray diffraction experiments [40,41]. The RDF of the aggregated nanoparticle shows that during aggregation the MgO nanoparticles continue to maintain their crystalline form. Furthermore, the bonding between the MgO is so highly directed, resulting in a continuous structure. Thus although the overall shape is non-symmetric there are no obvious grain boundaries being formed. Next we show the aggregation process of eight calcite nanoparticles.

12. Aggregation of calcite nanoparticles

Eight calcite nanoparticles that are 1.6 nm in diameter are placed 1.7 nm apart. The starting configuration is shown in figure 25. The simulation was run for 1 ns. Figure 26 shows the potential energy of the system as a function of MD time. The simulation starts with a potential energy of − 715.3 kJ/mol of calcium ions. As the simulation evolves the first drop in potential energy occurs at around 50 ps. This corresponds to figure 27 which shows that before aggregation occurs the individual nanoparticles will relax

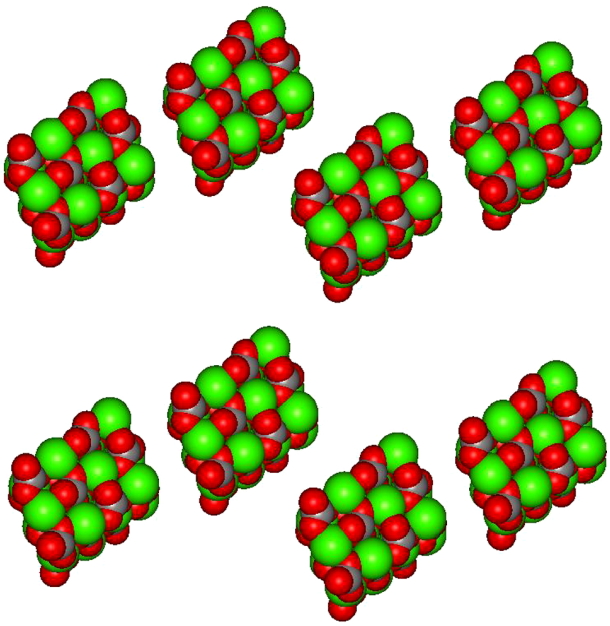

Figure 25. Initial configuration of calcite nanoparticles for MD simulation.

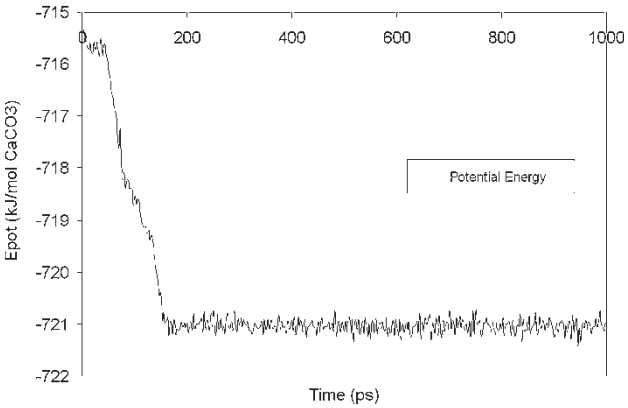

Figure 26. Potential energy per calcium ion against time of an MD simulation of eight calcite nanoparticles.

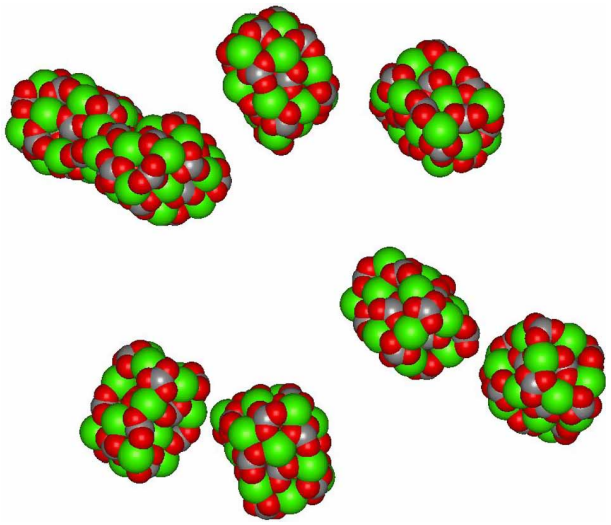

Figure 27. A snapshot of the MD simulation at 50 ps for the calcite 1.6 nm system.

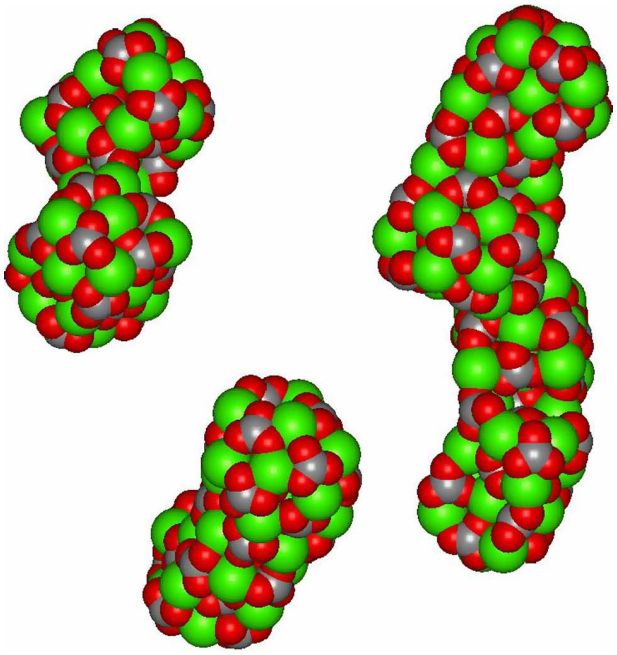

Figure 28. A snapshot of the MD simulation at 87 ps for the calcite 1.6 nm system.

Downloaded At: 17:58 14 January 2011

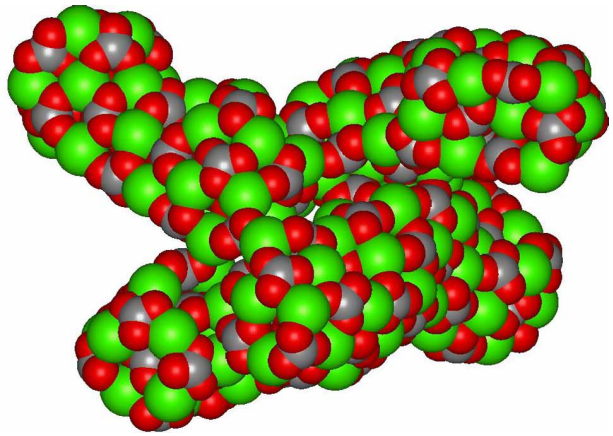

Figure 29. A snapshot of the MD simulation at 140 ps for the calcite 1.6 nm system.

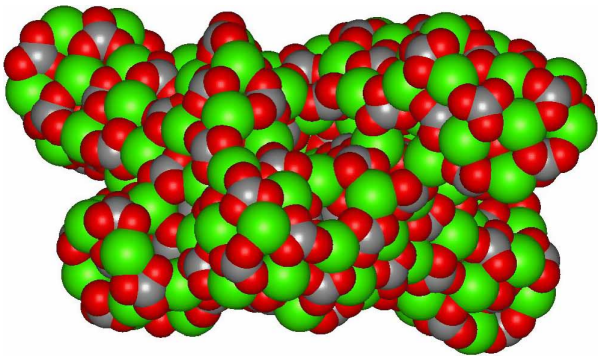

Figure 30. Final configuration of the aggregated calcite nanoparticles.

on their own to a potential energy of −715.6 kJ/mol, which corresponds to a more disordered structure. Once the calcite particles are relaxed aggregation occurs in pairs. At around 67 ps the eight nanoparticles have formed four nanoparticles and the energy lowers to −716.9 kJ/mol. Figure 28 shows a snapshot of aggregation at 87 ps. The potential energy of this system continues to lower, −718.2 kJ/mol, as the four calcite nanoparticles start to form two larger nanocrystals. The two larger calcite nanoparticles now become attracted to each other and again as they merge the potential energy drops to −719.9 kJ/mol at around 140 ps (figure 29). The final configuration occurs at 180 ps and the potential energy stabilises at −721.0 kJ/mol. Figure 30 shows the aggregated nanoparticle, which has lost its symmetry. The final nanoparticle has a longest diameter of 4.17 nm and a width of 1.816 nm. Figure 31(a) shows the RDF of the final aggregated calcite nanoparticle. When compared

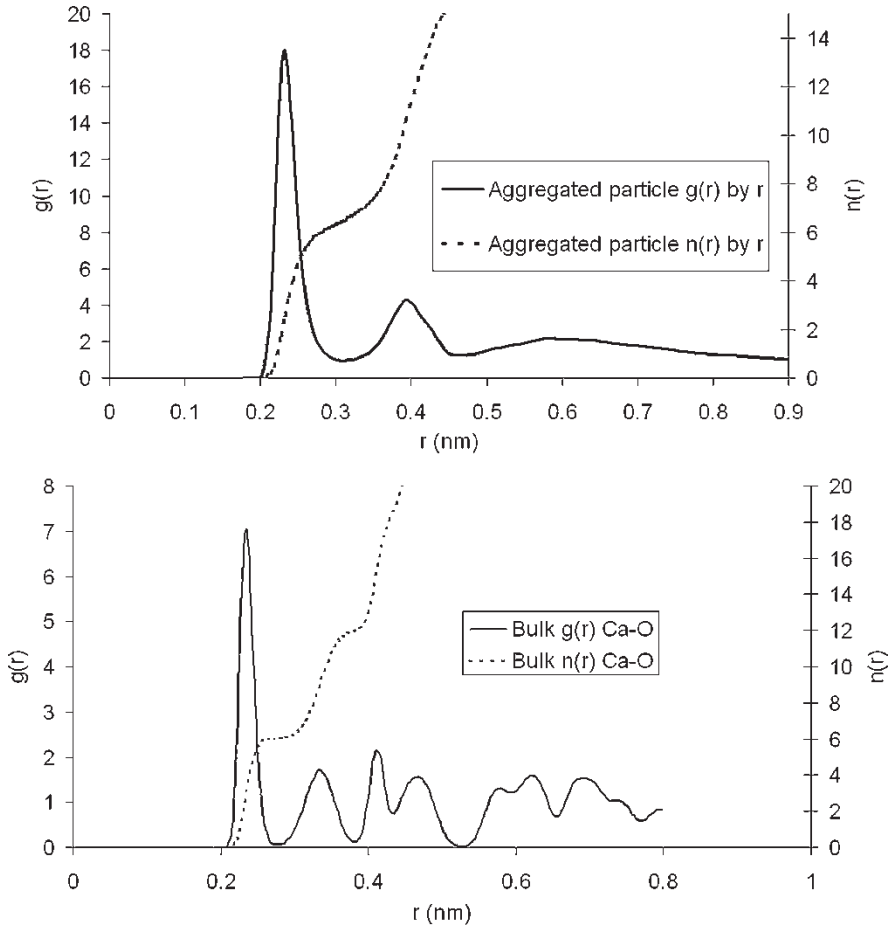

Figure 31. RDF of the (a) aggregated calcite nanoparticles and (b) bulk calcite.

Downloaded At: 17:58 14 January 2011

with the RDF of bulk calcite (figure 31(b)) it has much less order and is more amorphous then the crystalline bulk. The peaks in the RDF bulk calcite shows the same Ca—O bond distances, 0.23, 0.33, 0.41 nm, as found experimentally [42,43]. The average coordination number for a calcium ion in the aggregated nanoparticle is calculated to be around 6.5, which is slightly higher then the coordination number for bulk calcite which is 6. This suggests that the amorphous nanoparticle is more closely related to calcite, rather than aragonite which has a calcium ion coordination number of 8.

The difference between an aggregated calcite and an aggregated MgO is that MgO keeps its bulk-like structure and still has crystalline characteristics. The RDF shows sharp peaks whereas the RDF of the aggregated calcite is more amorphous with only two peaks. The atoms of the calcite nanoparticle seems to be more disordered and has no structural preference for linking different particles whereas the aggregated MgO has a very uniform structure.

There has been a great deal of debate in the literature suggesting that biomineralisation occurs from amorphous calcium carbonate [44–47]. We have shown that very small calcium carbonate nanoparticles are more stable when amorphous and also when they aggregate together their morphology changes drastically. Therefore this aggregation process could promote the exotic morphologies seen in biomineralistion. In future studies we set out to quantify this aggregation process.

Downloaded At: 17:58 14 January 2011

13. Conclusions

DL_POLY has great scope for our MD simulation experiments. We have been able to calculate both the free energy of nanoparticle aggregation and the activation free energy of individual atom migration. DL_POLY has also been shown to be versatile when used as an energy optimiser and for investigating adsorption of molecules on surfaces.

Application of DL_POLY has allowed us to investigate oxygen atom migration at the stable {111} surface of ceria. The oxygen migration is shown to be much more energetically favoured at the {111} surface than the bulk when via subsurface oxygen vacancies, and the activation free energy of migration was found to be the same in all directions. When considering the effect of neighbouring charge compensating Ce^{3+} ions the oxygen was found to be less mobile and no longer isotopic.

We have determined the adsorption energy and sites of the 76 PCDD congeners on a pyrophilite surface, using DL_POLY. The molecules are weakly bonded and the corrugation is low. The variation in energy with adsorption sites is small. The main factor controlling the adsorption energy is the number of chlorine atoms.

The simplicity of the PCDDs adsorption on this surface means that the process can be modelled very simply and parameterised for use in large scale soil remediation models.

We have investigated the differences between calcite and MgO nanoparticle aggregation. The difference between an aggregated calcite and an aggregated MgO is that MgO keeps its bulk-like structure and aggregates in specific orientations. In contrast, aggregated calcite is more amorphous and does not have any noticeable preferred directionality. The structure of the calcite nanoparticle seems to be more mobile whereas the aggregated MgO has a very uniform structure.

In summary, DL_POLY allows us to carry-out sophisticated MD simulations, intricate computational calculations and gives us scope for further investigatory work. Importantly, these applications of DL_POLY are providing a useful complement to experiments.

References

[1] T.O. White, R.P. Bruin, J. Wakelin, C. Chapman, D. Osborn, P. Murray-Rust, E. Artacho, M.T. Dove, M. Calleja. eScience methods for the combinatorial chemistry problem of adsorption of pollutant organic molecules on mineral surfaces. *Proceedings of the UK e-Science All Hands Meeting 2006* (2005).

[2] G.A. Deluga, J.R Salge, L.D. Schmidt, X.E. Verykios. Renewable hydrogen from ethanol by autothermal reforming. *Science*, **303**, 5660 (2004).

[3] K. Otsuka, T. Ushiyama, I. Yamanaka. Partial oxidation of methane using the redox of cerium oxide. *Chem. Lett.*, 9 (1993).

[4] Trovarelli, *Catalysis by Ceria and Related Materials*, Imperial College Press, London (2002).

[5] S.D. Park, J.M. Vohs, R.J. Gorte. Direct oxidation of hydrocarbons in a solid-oxide fuel cell. *Nature*, **404**, 6775 (2000).

[6] G.W. Watson, E.T. Kelsey, N.H. deLeeuw, D.J. Harris, S.C. Parker. Atomistic simulation of dislocations, surfaces and interfaces in MgO. *J. Chem. Soc. Faraday Trans.*, **92**, 3 (1996).

[7] G. Balducci, J. Kaspar, P. Fornasiero, M. Graziani, M.S. Islam, J.D. Gale. Computer simulation studies of bulk reduction and oxygen migration in CeO2−ZrO2 solid solutions. *J. Phys. Chem. B*, **101**, 10 (1997).

[8] T.X.T. Sayle, S.C. Parker, C.R.A. Catlow. Surface segregation of metal−ions in cerium dioxide. *J. Phys. Chem.*, **98**, 51 (1994).

[9] A.W. Dick, B.G. Overhauser. Theory of dielectric constants of alkali halide crystals. *Phys. Rev.*, **112**, 1 (1958).

[10] S. Kerisit, S.C. Parker. Free energy of adsorption of water and metal ions on the {1014} calcite surface. *J. Am. Chem. Soc.*, **126**, 32 (2004).

[11] G. Balducci, M.S. Islam, J. Kaspar, P. Fornasiero, M. Graziani. Bulk reduction and oxygen migration in the ceria-based oxides. *Chem. Mater.*, **12**, 3 (2000).

[12] D.J. Harris, M.Y. Lavrentiev, J.H. Harding, N.L. Allan, J.A. Purton. Novel exchange mechanisms in the surface diffusion of oxides. *J. Phys. Condensed Matter*, **16**, 13 (2004).

[13] M. Nolan, S. Grigoleit, D.C. Sayle, S.C. Parker, G.W. Watson. Density functional theory studies of the structure and electronic structure of pure and defective low index surfaces of ceria. *Surf. Sci.*, **576**, 1 (2005).

[14] M. Nolan, S.C. Parker, G.W. Watson. The electronic structure of oxygen vacancy defects at the low index surfaces of ceria. *Surf. Sci.*, **595**, 1 (2005).

[15] M. Nolan, S.C. Parker, G.W. Watson. Reduction of NO2 on ceria surfaces. *J. Phys. Chem. B*, **110**, 5 (2006).

[16] M. Nolan, S.C. Parker, G.W. Watson. CeO2 catalysed conversion of CO, NO2 and NO from first principles energetics. *Phys. Chem. Chem. Phys.*, **8**, 2 (2006).

[17] S.C. Parker, S. Kerisit, A. Marmier, S. Grigoleit, G.W. Watson. Modelling inorganic solids and their interfaces: a combined approach of atomistic and electronic structure simulation techniques. *Faraday Discuss.*, **124** (2003).

[18] G.L. Keldsen, J.B. Nicholas, K.A. Carrado, R.E. Winans. Molecular modeling of the enthalpies of adsorption of hydrocarbons on smectite clay. *J. Phys. Chem.*, **98**, 1 (1994).

[19] N.T. Skipper, P.A. Lock, J.O. Titiloye, J. Swenson, Z.A. Mirza, W.S. Howells, F. Fernandez-Alonso. The structure and dynamics of 2-dimensional fluids in swelling clays. *Chem. Geol.*, **230**, 3 (2006).

[20] C.H. Yu, S.Q. Newton, M.A. Norman, L. Schafer, D.M. Miller. Molecular dynamics simulations of adsorption of organic compounds at the clay mineral/aqueous solution interface. *Struct. Chem.*, **14**, 2 (2003).

[21] Q.H. Zeng, A.B. Yu, G.Q. Lu, R.K. Standish. Molecular dynamics simulation of organic-inorganic nanocomposites: layering behavior and interlayer structure of organoclays. *Chem. Mater.*, **15**, 25 (2003).

[22] G.V. Lewis, C.R.A. Catlow. Potential models for ionic oxides. *J. Phys. C Solid State Phys.*, **18**, 6 (1985).

[23] P. Dauberosguthorpe, V.A. Roberts, D.J. Osguthorpe, J. Wolff, M. Genest, A.T. Hagler. Structure and energetics of ligand-Binding to proteins—*Escherichia-Coli* dihydrofolate reductase trimethoprim, a drug-receptor system. *Proteins Struct. Funct. Genet.*, **4**, 1 (1988).

[24] M.J. Frisch, G.W. Trucks, H.B. Schlegel, G.E. Scuseria, M.A. Robb, J.R. Cheeseman, J. Montgomery, J.A.T. Vreven, K.N. Kudin, J.C., J.M. Millam, S.S. Iyengar, J. Tomasi, V. Barone, B. Mennucci, M. Cossi, G. Scalmani, N. Rega, G.A. Petersson, H. Nakatsuji, M. Hada, M. Ehara, K. Toyota, R. Fukuda, J. Hasegawa, M. Ishida, T. Nakajima, Y. Honda, O. Kitao, H. Nakai, M. Klene, X. Li, J.E. Knox, H.P. Hratchian, J.B. Cross, V. Bakken, C. Adamo, J. Jaramillo, R. Gomperts, R.E. Stratmann, O. Yazyev, A.J. Austin, R. Cammi, C. Pomelli, J.W. Ochterski, P.Y. Ayala, K. Morokuma, G.A. Voth, P. Salvador, J.J. Dannenberg, V.G. Zakrzewski, S. Dapprich, A.D. Daniels, M.C. Strain, O. Farkas, D.K. Malick, A.D. Rabuck, K. Raghavachari, J.B. Foresman, J.V. Ortiz, Q. Cui, A.G. Baboul, S. Clifford, J. Cioslowski, B.B. Stefanov, G. Liu, A. Liashenko, P. Piskorz, I. Komaromi, R.L. Martin, D.J. Fox, T. Keith, M.A. Al-Laham, C.Y. Peng, A. Nanayakkara, M. Challacombe, P.M.W. Gill, B. Johnson, W. Chen, M.W. Wong, C. Gonzalez, J.A. Pople. *Gaussian 03, Revision C.02*, Gaussian, Inc., Wallingford CT (2004).

[25] A.I. Zhukova, S.V. Bondarenko, Y.I. Tarasevich. Study of selectivity of natural sorbents with respect to hydrocarbons. *Ukr. Khim. Zh.*, **42**, 7 (1976).

[26] W. Smith, T.R. Forester. DL_POLY_2.0: a general-purpose parallel molecular dynamics simulation package. *J. Mol. Graph.*, **14**, 3 (1996).

[27] J.D. Gale, A.L. Rohl. The general utility lattice program (GULP). *Mol. Simul.*, **29**, 5 (2003).

[28] E. Spano, S. Hamad, C.R.A. Catlow. Computational evidence of bubble ZnS clusters. *J. Phys. Chem. B*, **107**, 38 (2003).

[29] E. Spano, S. Hamad, C.R.A. Catlow. ZnS bubble clusters with onion-like structures. *Chem. Commun.*, 7 (2004).

[30] H.Z. Zhang, F. Huang, B. Gilbert, J.F. Banfield. Molecular dynamics simulations, thermodynamic analysis, and experimental study of phase stability of zinc sulfide nanoparticles. *J. Phys. Chem. B*, **107**, 47 (2003).

[31] H.Z. Zhang, B. Gilbert, F. Huang, J.F. Banfield. Water-driven structure transformation in nanoparticles at room temperature. *Nature*, **424**, 6952 (2003).

[32] H.Z. Zhang, J.F. Banfield. Aggregation, coarsening, and phase transformation in ZnS nanoparticles studied by molecular dynamics simulations. *Nano Lett.*, **4**, 4 (2004).

[33] G.V. Lewis, C.R.A. Catlow. Potential model for ionic oxides. *J. Phys. Chem. Solid State Phys.*, **18** (1985).

[34] N.H. de Leeuw, S.C. Parker. Molecular-dynamics simulation of MgO surfaces in liquid water using a shell-model potential for water. *Phys. Rev. B*, **58**, 20 (1998).

[35] D.J. Harris, J.H. Harding, S.C. Parker. Simulations of surfaces and interfaces in MgO. *Radiation Effects and Defects in Solids*, **151**, 1 (1999).

[36] D.C. Sayle, J.A. Doig, S.A. Maicaneanu, G.W. Watson. Atomistic structure of oxide nanoparticles supported on an oxide substrate. *Phys. Rev. B*, **65**, 24 (2002).

[37] A. Pavese, M. Catti, S.C. Parker, A. Wall. Modelling of the thermal dependence of structural and elastic properties of calcite, $CaCO_3$. *Phys. Chem. Min.*, **23**, 2 (1996).

[38] S. Kerisit, S.C. Parker. Free energy of adsorption of water and calcium on the {10(1)over-bar-4} calcite surface. *Chem. Commun.*, 1 (2004).

[39] S. Kerisit, D.J. Cooke, D. Spagnoli, S.C. Parker. Molecular dynamics simulations of the interactions between water and inorganic solids. *J. Mater. Chem.*, **15**, 14 (2005).

[40] W.L. Bragg. Crystal structure. *Nature*, **105** (1920).

[41] V.G. Tsirel'son, A.S. Avilov, Yu.A. Abramov, E.L. Belokoneva, R. Kitaneh, D. Feil. X-ray and electron diffraction study of Mg O. *Acta Crystallogr. B*, **54** (1998).

[42] E.N.S.t. Maslen, V.A. Streltsov, N.R. Strel'tsova. X-ray study of the electron density in calcite, $CaCO_3$. *Acta Crystallogr. B*, **49** (1993).

[43] R.W.G. Wyckoff. The crystal structures of some carbonates of the calcite group. *Am. J. Sci. Serie*, **50** (1920).

[44] L. Addadi, S. Raz, S. Weiner. Taking advantage of disorder: amorphous calcium carbonate and its roles in biomineralization. *Adv. Mater.*, **15**, 12 (2003).

[45] M. Faatz, F. Grohn, G. Wegner. Amorphous calcium carbonate: synthesis and potential intermediate in biomineralization. *Adv. Mater.*, **16**, 12 (2004).

[46] S. Weiner, Y. Levi-Kalisman, S. Raz, L. Addadi. Biologically formed amorphous calcium carbonate. *Connect. Tissue Res.*, **44** (2003).

[47] X.R. Xu, J.T. Han, K. Cho. Formation of amorphous calcium carbonate thin films and their role in biomineralization. *Chem. Mater.*, **16**, 9 (2004).

Downloaded At: 17:58 14 January 2011